Lagrangian Droplet Dynamics in the Subsiding Shell of a Cloud Using Direct Numerical Simulations

VINCENT E. PERRIN AND HARMEN J. J. JONKER

Delft University of Technology, Delft, Netherlands

(Manuscript received 12 February 2015, in final form 28 May 2015)

ABSTRACT

This study investigates the droplet dynamics at the lateral cloud–environment interface in shallow cumulus clouds. A mixing layer is used to study a small part of the cloud edge using direct numerical simulation combined with a Lagrangian particle tracking and collision algorithm. The effect of evaporation, gravity, coalescence, and the initial droplet size distribution on the intensity of the mixing layer and the evolution of the droplet size distribution is studied. Mixing of the droplets with environmental air induces evaporative cooling, which results in a very characteristic subsiding shell. As a consequence, stronger horizontal velocity gradients are found in the mixing layer, which induces more mixing and evaporation. A broadening of the droplet size distribution is observed as a result of evaporation and coalescence. Gravity acting on the droplets allows droplets in cloudy filaments detrained from the cloud to sediment and remain longer in the unsaturated environment. While this effect of gravity did not have a significant impact in this case on the mean evolution of the mixing layer, it does contribute to the broadening of the droplet size distribution and thereby significantly increases the collision rate. Although more but smaller droplets result in more evaporative cooling, more droplets also increase small-scale fluctuations and the production of turbulent dissipation. For the smallest droplets considered with a radius of 10 μm, the authors found that, although a more pronounced buoyancy dip was present, the increase in dissipation rate actually led to a decrease in the turbulent intensity of the mixing layer. Extrapolation of the results to realistic clouds is discussed.

1. Introduction

For many decades, scientists have been interested in the microphysical processes inside a cloud. Much effort is dedicated to understand how droplets form and evolve and how rain is formed. One of the unresolved problems in cloud physics is to explain the rapid growth of cloud droplets in the size range 15–40 μm in radius for which neither the diffusional mechanism nor the gravitational collision–coalescence mechanism is effective (Grabowski and Wang 2013), known as the condensation–coalescence bottleneck or the size gap. One of the difficulties of understanding a cloud is that all scales are intrinsically linked, and the lack of realistic cloud models that span all the relevant scales makes it difficult to predict both the cloud lifetime and the time it takes for a cloud to rain (Devenish et al. 2012).

Numerous studies have been dedicated to understand the role of turbulence on the collision kernel. While most studies using direct numerical simulations (DNSs) report an increased collision rate as compared to nonturbulent flows, the results cannot be extrapolated easily to realistic atmospheric conditions. Devenish et al. (2012) argue that most DNS studies are idealized and that it is difficult to determine what the relevant parameters are and also their values in realistic clouds. Indeed many DNS studies have been conducted without gravity, at moderate Reynolds numbers, for much higher energy dissipation rates than is typical of clouds, for a monodisperse droplet distribution, and for relatively high droplet concentrations compared with typical concentrations in clouds. Most of the studies also study the droplet dynamics in homogeneous and isotropic turbulence.

Two mechanisms can be identified that are responsible for the broadening of the droplet size distribution (DSD). The first mechanism is the exchange of mass and heat between the droplet and its surroundings through condensation (evaporation), which allows them

Corresponding author address: Harmen J. J. Jonker, Delft University of Technology, Stevinweg 1, Delft 2628 CN, Netherlands.
E-mail: h.j.j.jonker@tudelft.nl

DOI: 10.1175/JAS-D-15-0045.1

to grow (shrink). Condensation is a very important process in the early stages of cloud evolution, since it is the only effective growth mechanism for droplets of a few micrometers (Pruppacher and Klett 1978). The second mechanism broadening the DSD is coalescence, which is governed by the collision rate. Both broadening mechanisms are coupled, since the broadening of the DSD in warm cumulus clouds by evaporation and condensation alters the collision rate.

Small-scale turbulence alone fails to reproduce the observed broadening of the droplet size distributions (Vaillancourt et al. 2002; Lanotte et al. 2009). Although at those scales preferential concentration contributes to an increase in the collision rate, it does not seem a good candidate to explain the observed broadening of the DSD in adiabatic cloud cores. Different mechanisms have been proposed to explain the broadening of the DSD (Jonas 1996; Shaw 2000; Pinsky and Khain 2002; Kostinski and Shaw 2005; Korolev et al. 2013) in adiabatic cloud cores. Results from Lanotte et al. (2009) show that the DSD broadens faster for increasing Reynolds numbers, which emphasizes the need for cloud models that span all the relevant scales.

The broadening of the DSD has also been studied at the cloud–environment interface where unsaturated environmental air mixes with the humid cloud air that allows droplets to evaporate (Jonas 1996; Andrejczuk et al. 2004; Lasher-Trapp et al. 2005; Andrejczuk et al. 2006; Korczyk et al. 2006; Andrejczuk et al. 2009; Lehmann et al. 2009; Jones et al. 2010; Kumar et al. 2013; Grabowski and Wang 2013; Tölle and Krueger 2014; Kumar et al. 2014; Babkovskaia et al. 2015). All studies agree that the amount of cloud–environment mixing is positively correlated with the amount of evaporation and broadening of the DSD.

Latent heat release by condensation in clouds is a very important source for generating positive buoyancy (Wallace and Hobbs 2006). Evaporating droplets on the contrary generate negative buoyancy, which at the top of a cloud generates cloud-top instability (Deardorff 1980; Mellado et al. 2009; Mellado 2010) or at cloud edge creates a negatively buoyant cloud shell (Heus and Jonker 2008; Jonker et al. 2008; Heus et al. 2009; Wang and Geerts 2010; Abma et al. 2013; Katzwinkel et al. 2014). As a result, evaporation increases the level of turbulence and broadens the droplet size distribution.

In this paper we will investigate the lateral boundary of shallow cumulus clouds using DNS with a comparable approach as Abma et al. (2013). Our study differs in two important aspects. First, the initial profiles used by Abma et al. (2013) are idealized in the sense that the inner part of the cloud is taken to be neutrally buoyant with respect to the environment, whereas the clouds in this study have a positive buoyancy. The second and more important difference is that we use a Lagrangian particle tracking to follow all droplets individually and compute their interaction with their surroundings. This approach allows us to investigate the effect of evaporation, condensation, and coalescence on the evolution of the DSD.

By using a developing mixing layer as a paradigm for a small portion of the edge of a cloud, we will address two questions in this paper. We will first investigate the role of evaporation, gravity, and coalescence on the turbulent intensity of the mixing layer and its mean velocity and buoyancy profiles. Second, we will investigate the broadening of the droplet size distribution and to what extent fast droplet growth through coalescence can occur.

This paper is outlined in the following way. Section 2 briefly treats the theoretical background of evaporation droplets in turbulent flows, followed by the numerical details of the DNS in section 3. The results of this study will be presented and discussed in section 4. A discussion on the extrapolation of the results to realistic clouds is added in section 5. Conclusions of this paper are provided in section 6.

2. Background

a. Droplet growth and condensation rate

The exchange of heat and moisture between the droplets and the environment can be calculated explicitly by solving a set of three convective–diffusive equations for the water vapor and the temperature inside and outside the droplet. The growth of cloud droplets can be parameterized as a function of the local air conditions using the steady-state wet-bulb temperature, since the time scales associated with the droplet temperature response is much smaller than the time scale associated with the change in ambient conditions (Vaillancourt et al. 2001). For droplets smaller than 30 μm, convective transport only plays a small role and can be neglected (Sedunov and Greenberg 1974; Pruppacher and Klett 1978). The growth equation for the droplet with radius r is therefore given by

$$\frac{dr^2}{dt} = 2KS, \tag{1}$$

where S is the supersaturation of the local flow field, defined in terms of the vapor pressure e, and is given by $S = e/e_{\mathrm{sat}}(T) - 1$. The term "local" refers to the grid value provided by the DNS. The equilibrium vapor pressure e_{sat} is computed using the August–Roche–Magnus approximation (Alduchov and Eskridge 1996).

TABLE 1. Overview of the value of the physical constants used.

Constant	Value
ρ_f	$1.14\,\mathrm{kg\,m^{-3}}$
ρ_p	$1.0\times10^{3}\,\mathrm{kg\,m^{-3}}$
L	$2.5\times10^{6}\,\mathrm{J\,kg^{-1}}$
R_v	$461.5\,\mathrm{J\,kg^{-1}\,K^{-1}}$
k_a	$2.22\times10^{-5}\,\mathrm{m^2\,s^{-1}}$
D_v	$2.55\times10^{-5}\,\mathrm{m^2\,s^{-1}}$
ν	$1.5\times10^{-5}\,\mathrm{m^2\,s^{-1}}$
g	$9.81\,\mathrm{m\,s^{-2}}$

The evaporation rate for cloud droplets is given by (Pruppacher and Klett 1978)

$$K^{-1}=\frac{\rho_p R_v T}{e_{\mathrm{sat}}(T)D_v}+\frac{L\rho_p}{k_a T}\left(\frac{L}{R_v T}-1\right), \tag{2}$$

where R_v is the gas constant for water, D_v is the molecular diffusivity of water, L is the latent heat of vaporization of water, ρ_p is the density of the droplets, T is the temperature, and k_a is the thermal diffusivity of air. See Table 1 for an overview of the constants used.

b. Droplet dynamics and collision statistics

If the density of the droplets is high compared to the density of the air ρ_f and if the droplet radius is small compared to the Kolmogorov scale $\eta=(\nu^3/\langle\epsilon\rangle)^{1/4}$ of the flow, computed from the mean dissipation rate $\langle\epsilon\rangle$ and the kinematic viscosity of the air ν, the full equations of motion of particles in turbulence (Maxey and Riley 1983; Gatignol 1983) can be reduced to

$$\frac{d\mathbf{v}(t)}{dt}=\frac{\mathbf{u}[\mathbf{x}(t),t]-\mathbf{v}(t)}{\tau_p}+\mathbf{g}\quad\text{and} \tag{3}$$

$$\frac{d\mathbf{x}(t)}{dt}=\mathbf{v}(t), \tag{4}$$

where $\mathbf{u}$ represents the velocity vector of the flow field, $\mathbf{v}$ represents the velocity vector of a droplet, and $\mathbf{x}$ represents the position vector of a droplet. Under the assumption of Stokes drag, $\tau_p=2\rho_p r^2/(9\rho_f\nu)$ is the droplet relaxation time. The last term in Eq. (3), $\mathbf{g}$, is the gravitational acceleration and $g=|\mathbf{g}|$. The response of the droplets to the flow can be described by the Stokes number:

$$\mathrm{St}=\frac{\tau_p}{\tau_\eta}, \tag{5}$$

where $\tau_\eta=(\nu/\langle\epsilon\rangle)^{1/2}$ is the Kolmogorov time scale. In the presence of gravity, we can define the fluid Froude number as $\mathrm{Fr}=\epsilon^{3/4}/(g\nu^{1/4})$, which is a nondimensional measure for the turbulence intensity compared to the strength of the gravity.

In cloudlike conditions, where the Weber number (We) is very low $[O(10^{-2})]$, colliding droplets generally coalesce (Ashgriz and Poo 1990; Qian and Law 1997). In this study we therefore assume that all colliding droplets coalesce. The Weber number quantifies the relative importance of the fluid's inertia compared to its surface tension. For a matter of simplicity, we do not take into account the collisions efficiency of the droplets, although it can greatly influence the collision rate (Pinsky et al. 1999, 2001) and can vary from 0.01 to 1, depending on both droplet sizes and the surrounding pressure. In section 5 we will discuss the implications of this assumption for clouds.

The average number of collisions $\dot{\mathcal{N}}_{12}$ per unit volume and unit time between two arbitrary groups of droplets with radii r_1 and r_2 is given by

$$\dot{\mathcal{N}}_{12}=N_1N_2\Gamma_{12}, \tag{6}$$

where N_1 and N_2 are number concentrations of the two different groups and Γ_{12} is the collision kernel.

c. Flow field

Following the approach of Vaillancourt et al. (2001), we solve the coupled incompressible conservation equations for mass, momentum, temperature, and moisture for the flow field:

$$\nabla\cdot\mathbf{u}=0, \tag{7}$$

$$\frac{\partial\mathbf{u}}{\partial t}=-\mathbf{u}\cdot\nabla\mathbf{u}-\frac{1}{\rho_f}\nabla p+\nu\nabla^2\mathbf{u}+\mathbf{g}B, \tag{8}$$

$$\frac{\partial T}{\partial t}=-\mathbf{u}\cdot\nabla T+\frac{L}{c_p}C_d+k_a\nabla^2T,\quad\text{and} \tag{9}$$

$$\frac{\partial q_v}{\partial t}=-\mathbf{u}\cdot\nabla q_v-C_d+D_v\nabla^2q_v, \tag{10}$$

where p represents the pressure field, T is the temperature field, q_v is the water vapor specific humidity, C_d is the condensation rate, and c_p is the specific heat of air. The last term in Eq. (8), $\mathbf{g}B$, represents the buoyancy, where B is described by

$$B=\frac{T^*}{T_0}+0.608q_v^*-q_l^*, \tag{11}$$

where the asterisk indicates a deviation from the environmental value, T_0 is the temperature of the environment, and $q_l=[m_l/(m_a+m_v+m_l)]$ is the liquid water content computed from the droplet distribution (m_a, m_v, and m_l are, respectively, the masses of air, vapor, and liquid water inside a grid volume). The condensation rate is given by

$$C_d = \frac{1}{m_a + m_v + m_l} 4\pi\rho_p KS \sum_{i=1}^{N_{p,g}} r_i, \tag{12}$$

where r_i is the radius of droplet with index i and $N_{p,g}$ is the number of droplets inside a single computational grid box (which may vary from one grid box to another).

d. Transition length scale

The Damköhler number (Da), defined as the ratio of the time scale of mixing and a thermodynamic reaction time scale, quantifies the characteristics of a mixing process. For a very low Damköhler number, the mixing of the carrier flow occurs very fast and all droplets experience the same thermodynamic forcings (homogeneous mixing). For a very high Damköhler number, the mixing of the carrier fluid is very slow and all droplets experience a different thermodynamic forcing (inhomogeneous mixing). For turbulent flows, however, mixing occurs on a continuous range of scales, ranging from the largest scales to the dissipation scales. Lehmann et al. (2009) therefore introduced the concept of the transition length scale. The transition length scales marks the boundary between homogeneous and inhomogeneous mixing at Da = 1. The transition length-scale l^* is defined as

$$l^* = \epsilon^{1/2} \tau_{\text{react}}^{3/2}, \tag{13}$$

where τ_{react} in this case is the droplet evaporation time scale τ_{evap}, given by

$$\tau_{\text{evap}} = \frac{r^2}{2KS}. \tag{14}$$

3. Numerical setup

To explicitly simulate the turbulence, we use a direct numerical simulation code (Jonker et al. 2013) to solve Eqs. (7)–(10) on a uniform staggered grid. The equations are discretized by the finite-volume method, with second-order central differences in space and second-order Adams–Bashforth in time. Time stepping is restricted by the Courant–Friedrich–Lewy criterion using a Courant number C of 0.25. The code also makes use of the MPI communication protocol as it is parallelized by domain decomposition in two dimensions, making the code highly scalable and fit for modern supercomputers.

The computational domain consist of a rectangle where the coordinate system is defined such that x, y, and z are the streamwise, wall-normal, and spanwise directions, respectively. The left part of the domain represents the cloud side, whereas the right part represents the neutrally buoyant environment. The domain is periodic in the streamwise and spanwise direction. Neumann boundary (free slip) conditions are used for the velocities, temperature, and moisture field, both in the cloud and in the environment. Gravity acts in the streamwise direction (i.e., x direction). The aim is to create a cloud-edge type of flow, where a humid buoyant parcel mixes with the dryer and neutrally buoyant environment.

The equations of motion [Eqs. (3) and (4)] of the droplets are updated using a fourth-order Runge–Kutta scheme, and the value of the velocity of the flow field at the droplet location $\mathbf{u}[\mathbf{x}(t), t]$ is obtained using trilinear interpolation.

The algorithm of Allen and Tildesley (1987) is used to detect collisions, which uses cell indexing and linked lists to check only droplet pairs that could collide within one time step [see also Chen et al. (1999) and Perrin and Jonker (2014)]. Coalescence can instantaneously be enacted if required. The new droplet radius is then computed based on mass conservation. The position of the new center of mass is computed as a weighted average of the two old centers of mass. Collisions between three droplets are not considered, since the time between collisions is several orders larger than the relaxation time of the droplets (Woittiez et al. 2009).

Updating the droplet radius using Eq. (1) using explicit methods requires a very small time step $\Delta t < 2\tau_{T_R}$, where τ_{T_R} is the relaxation time scale for the approach of the psychrometric temperature (droplet surface temperature) to its steady-state value. Especially for small droplets, this can be problematic. Therefore, the value of the mean supersaturation the droplets experience is computed using an implicit method (Hall 1980), in which the supersaturation is obtained by iteration using a Newton–Raphson method. This method consists of integrating the temperature and vapor field to an intermediate time step without the forcings of the droplets, which are the terms including C_d in Eqs. (9) and (10). Iteratively, the new supersaturation S^{t+1} and the new condensation rate C_d^{t+1} are locally computed, from which a new droplet radius is computed using the mean supersaturation $\overline{S} = (1/2)(S^t + S^{t+1})$. If the solution has not converged yet, in the next iteration, then a new local temperature and vapor can be computed with a new supersaturation rate and a new condensation rate. If the particle radius becomes smaller than 0.1 μm, then the droplet is removed.

A total of nine simulations has been performed, all including different physical processes (see Table 2 for more details). The first simulation ML1 is used as a reference without droplets. To simulation ML2 we add nonevaporative [i.e., $C_d = 0$ in Eqs. (9) and (10)] and

TABLE 2. Overview of the simulations, including the simulation name, the domain size L, the number of grid points N_x, and the physical processes droplets (d), evaporation (e), gravity (g), and coalescence (c).

Run	L(m)	N_x	N_p	r (μm)	d	e	g	c
ML1	$2\times1\times1$	$2048\times1024\times1024$	—	—				
ML2	$2\times1\times1$	$2048\times1024\times1024$	4×10^7	20	×			
ML3	$2\times1\times1$	$2048\times1024\times1024$	4×10^7	20	×	×		
ML4	$2\times1\times1$	$2048\times1024\times1024$	4×10^7	20	×	×	×	
ML5	$2\times1\times1$	$2048\times1024\times1024$	4×10^7	20	×			×
ML6	$2\times1\times1$	$2048\times1024\times1024$	4×10^7	20	×	×		×
ML7	$2\times1\times1$	$2048\times1024\times1024$	4×10^7	20	×	×	×	×
ML8	$2\times1\times1$	$2048\times1024\times1024$	9.5×10^7	15	×	×	×	×
ML9	$2\times1\times1$	$2048\times1024\times1024$	32×10^7	10	×	×	×	×

nonsedimentating droplets [i.e., $g=0$ in Eq. (3)]. In simulation ML3 we allow droplets to evaporate by computing their condensation rate using Eq. (12). In simulation ML4 we include the effect of gravity on the droplets and set $g=9.81\,\mathrm{m\,s^{-2}}$ in Eq. (3). In previously mentioned simulations, collisions are detected but not enacted. Simulations ML5–ML7 are identical to simulations ML2–ML4, but now all colliding droplets coalesce. All simulations have a uniform grid spacing of 1 mm and are carried out to provide more insight in which physical processes contribute to broadening of the droplet size distribution. The grid spacing used guarantees a minimum resolution of $\eta/\Delta x\geq1.4$ at the end of each simulation when the intensity of the turbulence is maximum. Simulations ML8 and ML9 are similar to simulation ML7, but with a different initial droplet size, but identical liquid water content.

The initial profiles for the prognostic variables used in all simulations are shown in Fig. 1 (left). The sharp interface is initially resolved with approximately 20 grid points. The cloud is slightly warmer and moister than the environment. This yields for simulation ML1 the diagnosed buoyancy and supersaturation profiles shown in Fig. 1 (right). Simulations ML2–ML9 have a slightly different buoyancy profile, since adding droplets changes the buoyancy B [see Eq. (11)]. Since our cloud edge is positively buoyant and has an upward velocity, one could speak of an actively growing cloud (Katzwinkel et al. 2014). The simulated time as been set to 15 s, which is approximately the time needed for the mixing layer to reach the computational boundaries.

The initial profiles have been chosen such that the supersaturation in the cloud does not exceed a few percent (Jonas 1996; Khain et al. 2007; Grabowski et al. 2011; Pinsky et al. 2013). The velocity in the streamwise direction has an identical shape as the profiles of temperature and humidity, with zero velocity in the environment and $40\,\mathrm{cm\,s^{-1}}$ in the cloud. The velocity in the spanwise and wall-normal direction has been set to zero. The initial velocity field at the interface in the wall-normal direction is perturbed with a small velocity perturbation of $0.001\,\mathrm{m\,s^{-1}}$.

A large number of droplets (see Table 2) is released at the beginning of the simulation in the cloud part of the domain, up to half of the domain size (i.e., from 0 to 50 cm). The number of droplets in all simulations corresponds to a value of the specific humidity $q_l\approx1\,\mathrm{g\,kg^{-1}}$.

4. Results

In this section we will analyze the effect of different physical processes on the evolution of the mixing layer. In all figures the same color coding is used. Distinctive features of each simulation are shown in parentheses in the legends (see Table 2 for the letter coding). We will first analyze simulations ML1–ML7. The angle brackets denote the volume average of a variable obtained by averaging over all grid points. Simulations ML8 and ML9 will be analyzed in the following subsection. Figure 2 (left) shows the evolution of the mean dissipation rate $\langle\epsilon\rangle$ and Fig. 2 (right) shows the evolution of the mean turbulent kinetic energy $\langle k\rangle$ (TKE), where $k=(1/2)\sqrt{u_1'^2+u_2'^2+u_3'^2}$. The velocity fluctuations u_1', u_2', and u_3' are defined as $u_i'=u_i-\langle u_i\rangle$. Figure 3 shows mean profiles in the wall-normal direction of the velocity (left panel) and the buoyancy (right panel) at $t=11$ s. All results presented here are averages based on 100 snapshots during 1 s. Please keep in mind that all results presented here are based on a single realization of each simulation.

We start with the simulation without droplets (black line) and gradually add physical processes and complexity. The buoyancy profile is such that the velocity in the cloud gradually increases until the mixing layer becomes unstable and starts to mix.

Adding nonevaporative droplets (simulations ML2 and ML5) decreases the buoyancy, according to Eq. (11), which also decreases the mean TKE and the mean dissipation rate (see Fig. 2). Evaporation (simulations

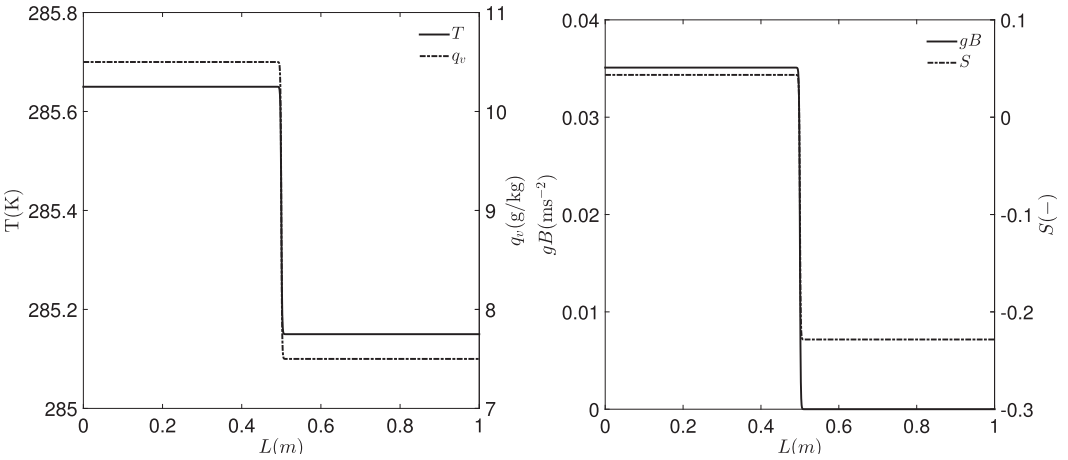

FIG. 1. (left) Initial profiles of the prognostic variables temperature T and humidity q_v of all simulations. (right) Initial profiles for the diagnosed buoyancy gB (excluding droplets) and supersaturation S.

ML3 and ML6) has a major impact on the evolution of the mixing layer. Latent heat release due to condensation in the cloud increases on a macroscale the buoyancy. On a microscale, buoyancy fluctuations result in an earlier instability. Outside the cloud, on the other hand, evaporative cooling results in a very characteristic dip in the buoyancy profile (Heus and Jonker 2008; Jonker et al. 2008; Heus et al. 2009; Wang and Geerts 2010; Abma et al. 2013; Katzwinkel et al. 2014). Condensation and evaporation near the edge of a cloud result in a larger horizontal buoyancy gradient across the cloud–environment interface, which results in more vorticity production (Grabowski 1989) and more instability. A positive feedback loop exists between the evaporation of droplets and the turbulent intensity of the mixing layer. Evaporation increases the level of turbulence and therefore the level of mixing, and a higher level of mixing yields more evaporation (Andrejczuk et al. 2009; Tölle and Krueger 2014).

Coalescence only has a minor impact on the flow mean properties and the flow is statistically identical. In our simulation setup gravity does not significantly affects the evolution of the mixing layer. However, subtle gravity effects as a result of small-scale changes could be washed away by the high turbulent intensity of the mixing layer.

Figure 4 shows a snapshot of the buoyancy field obtained from simulations ML5–ML7 at $t = 11$ s. The black regions of the flow represent regions of negative buoyancy. The black dots represent a local buoyancy decrease as a result of the presence of (multiple) droplets [see Eq. (11)]. Visually, it can be seen that gravity allows droplets in cloudy filaments detrained from the cloud to sediment and remain longer in the unsaturated environment. Multiple levels of mixing can also be identified.

So far we have looked at the role of evaporation and gravity on the evolution of the mixing layer from a macroscopic point of view. We will now focus on the droplet size distribution. Figure 5 (left) shows the DSD at $t = 11$ s. For the nonevaporative simulations, the distributions are shown with crosses. Note that the red cross is hidden underneath the left yellow cross. Evaporation significantly broadens the DSD and increases the occurrence of smaller droplets. The maximum droplet size through condensation is shown as a dotted vertical line. Droplet growth through condensation is only marginal since the droplets are relatively large and once the surplus of water vapor has condensed on the droplets at the beginning of the simulation, there is no mechanism to increase the supersaturation during the simulation since no adiabatic lapse rate is considered in our simulations. Figure 5 (right) shows the PDF of the supersaturation field conditionally sampled on the droplets location at $t = 11$ s.

As visually observed in Fig. 4, gravity allows droplets to remain longer in unsaturated air, which translates in a broader PDF of the supersaturation and a broadening of the DSD toward smaller sizes (see Fig. 6). Previous research by Kumar et al. (2013) also reported more evaporation at the cloud–environment interface in the presence of gravity. In merely 11 s, some droplets have grown from 20 to almost 30 μm through coalescence.

Figure 6 shows the PDF of the transition length scales obtained using Eq. (13) by sampling over all droplets. A broad range of scales can be observed. The most frequent transition length scale is approximately 3 m in the case of no gravity and approximately 0.5 m when gravity is included. The cases including gravity show a shift toward smaller length scales, indicating that mixing is more inhomogeneous. Since the mean dissipation rate is

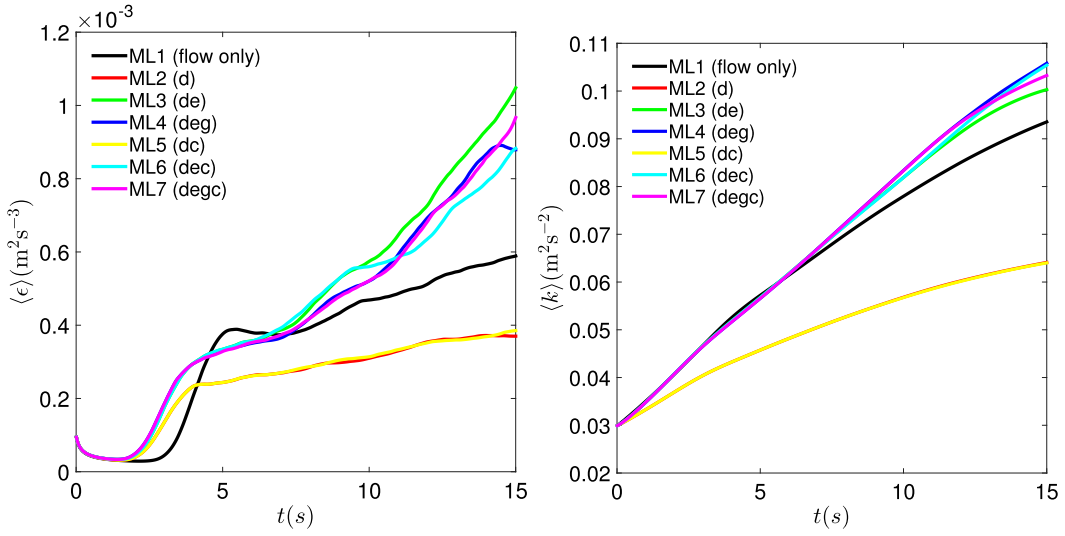

FIG. 2. Evolution of (left) the mean dissipation rate and (right) the mean turbulent kinetic energy during the simulation.

not significantly enhanced by gravity, this result supports the conclusion that gravity allows droplets to sedimentate into unsaturated air. Since coalesced droplets have a higher settling speed, this effect is only increased when coalescence is enacted. A transition length scale of 0.5 m is comparable to observations by Lehmann et al. (2009), where a length scale of approximately 0.1 m was found.

Figure 7 (right) shows the evolution of the collision kernel Γ_{12} throughout the simulations. The collision kernel is computed during the simulation based on the number of collisions and the number of droplets present [see Eq. (6)]. Evaporation increases the collision kernel, more than to be expected based on only the increase in turbulence intensity and dissipation rate (e.g., Ayala et al. 2008). This increase in collision kernel can be attributed to a broadening of the DSD. Droplets with a large size difference can have high relative radial velocity since they preferentially concentrate in different regions of the flow (e.g., Woittiez et al. 2009). Including gravity results in a substantially higher collision rate—a result of an even broader DSD. A broader DSD is the result of droplets being more exposed to unsaturated air. Qualitatively similar results were obtained by Kumar et al. (2013), where they concluded that droplets are exposed to very different vapor environments as a result of their inertia and gravitational settling. One can speculate from Fig. 4 that since gravity makes droplets in cloudy filaments sediment into an unsaturated environment, more evaporation is to be expected. This

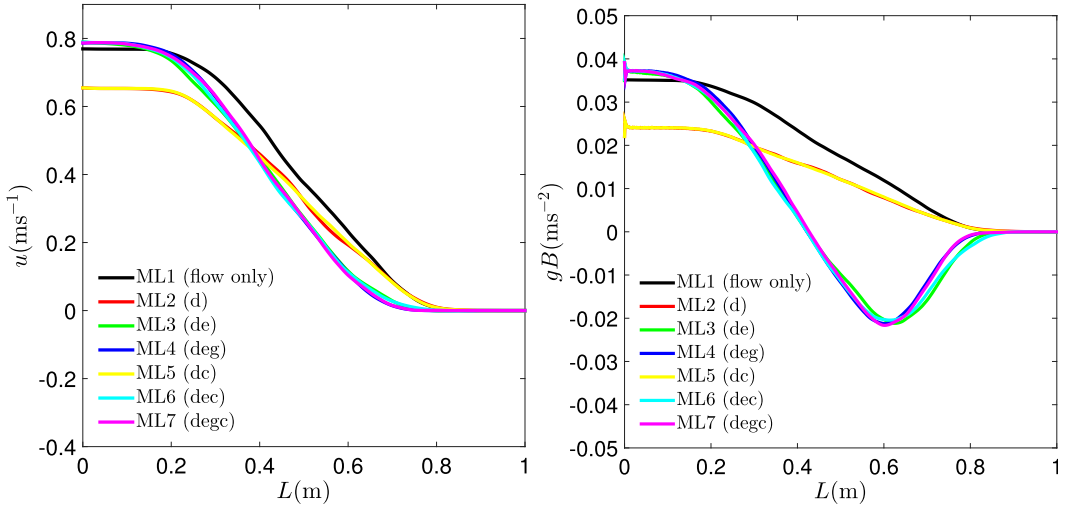

FIG. 3. (left) Average velocity profiles and (right) average buoyancy profiles across the mixing layer at $t = 11$ s.

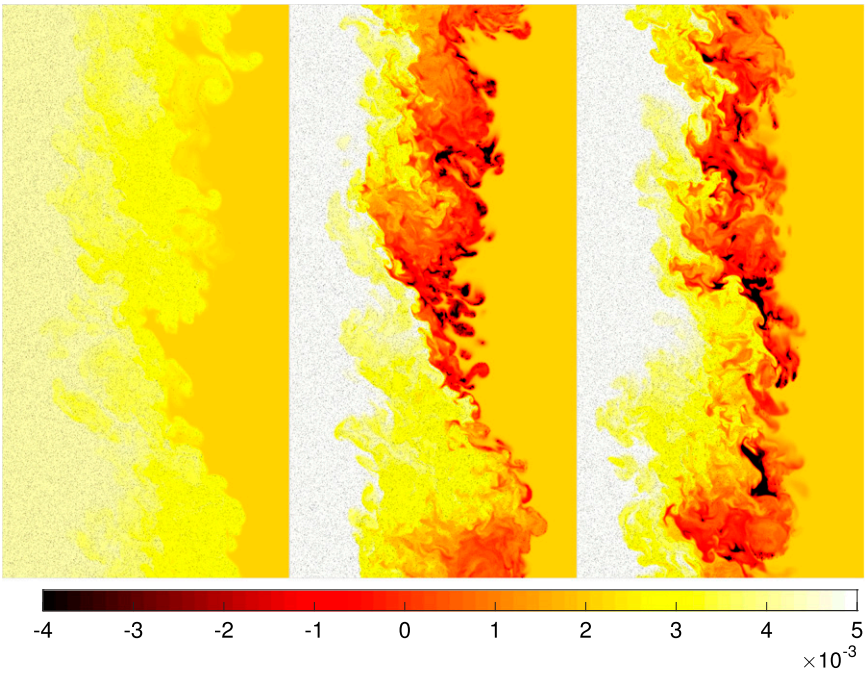

FIG. 4. Snapshot of the buoyancy field for simulations ML5–ML7 after 11 s. (left)–(right) Evaporation and gravity are added. Color bar is in 10^{-3} m s^{-2}.

additional evaporation is, however, not substantial enough in our simulations to significantly alter the mean velocity and buoyancy profiles (shown in Fig. 9). Coalescence reduces the collision kernel in absence of gravity because it reduces the local number of available droplets for collision. When gravity is included, it appears that the change in terminal velocity after coalescence compensates for this effect.

Figure 7 (left) shows the accumulated number of collisions throughout the mixing layer for different time periods. A moving-average filter with a span of 5 has been used to smooth the data. A higher number of collisions can be found near the cloud–environment interface. At the edge of the computational domain, the number of collisions is not higher than expected, indicating that turbophoresis does not play a significant role in this simulation. The inset shows the most frequent droplet radius at a certain wall-normal distance. Although more collisions occur at the interface, this does not imply that the maximum droplet radius is larger at that location during the simulation.

Effect of the droplet size distribution

In previous section, we have investigated the effect of evaporation, gravity, and coalescence on the properties of the mixing layer and of shape of the DSD. In this section we investigate the influence of the DSD itself on the evolution of the mixing layer. Simulations ML7–ML9 only differ in the initial radius of the droplets and all three simulations have identical liquid water content. Figure 8 shows the evolution of the mean dissipation rate and of the mean turbulent kinetic energy. Compared to a droplet radius of 20 μm, droplets with a radius of 15 μm generate more turbulent kinetic energy, but the dissipation rate remains similar, although it appears to start to grow earlier in the simulation. When the droplet size decreases even further to 10 μm, the dissipation rate drastically increases during the simulation and the mean TKE does not grow as fast. This is remarkable considering the fact that the buoyancy profile in Fig. 9 (left) is more pronounced for smaller droplets, which indicates that more evaporative cooling occurs. There appears to be a competition between evaporative cooling and the production of dissipation as a result of small-scale fluctuations.

Figure 9 (right) shows the collision kernel during the simulations normalized with the collisional cross-section $2\pi R_0^2$, where R_0 is the initial droplet size. Note that the mean droplet size during the simulation is very close to the initial droplet size (see Fig. 10). The larger the initial droplets are, the larger the collision kernel is. This is due to two different mechanisms. Larger droplets can detach more easily from the underlying flow field as a result of their momentum (Falkovich et al. 2002; Wilkinson and Mehlig 2005; Wilkinson et al. 2006; Falkovich and Pumir 2007), which allows larger relative velocities at small separation and results in more collisions. The second mechanism is the broadening of the DSD. Figure 10

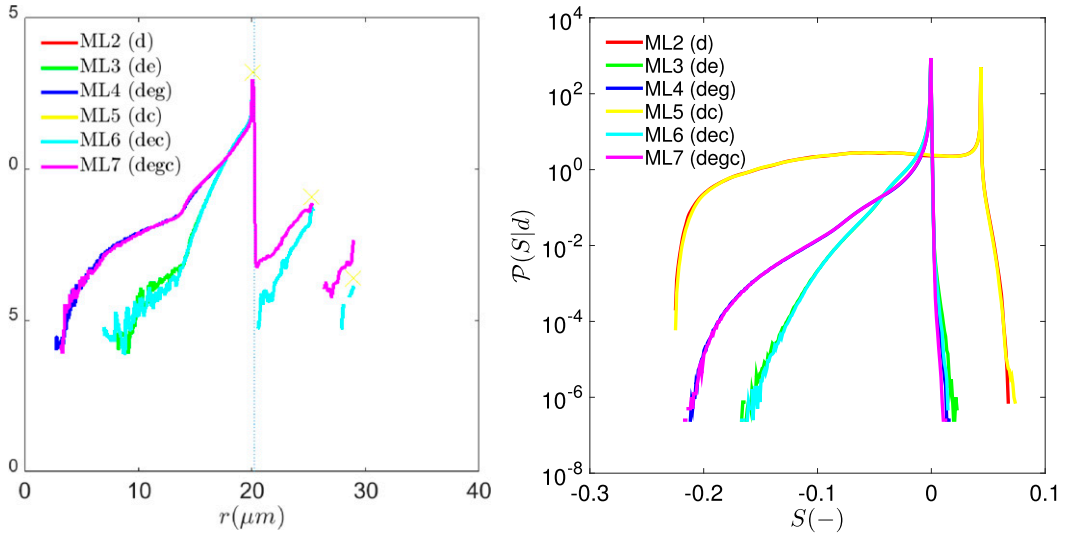

FIG. 5. (left) Probability density function of the DSD at $t = 11$ s. The vertical dotted line shows the maximum droplet size without coalescence by condensation only. Simulations without evaporations are indicated by crosses. Note that the red cross is hidden underneath the left yellow cross. (right) PDF of the supersaturation conditionally sampled on the droplet locations.

(left) shows the DSD at $t = 11$ s. The larger the initial droplet radius is, the broader the DSD becomes, which is favorable for collisions.

Figure 10 (right) shows the PDF of the supersaturation (dashed line) and the PDF of the supersaturation conditionally sampled on the droplets locations (solid line) at $t = 11$ s for simulations ML7–ML9. For similar liquid water content, the smaller the droplets are, the faster phase transition can occur, which allows the flow and the droplets to reach a thermodynamic equilibrium more quickly. Using this line of argument, we can partly understand why smaller droplets reside in regions of less unsaturated air. On top of that, as we have seen in Fig. 7, gravity also tends to broaden the PDF toward larger values of negative supersaturation. The larger the droplets are, the larger this broadening is expected to be.

5. Discussion

In this section we will discuss the applicability of the results found in the previous section to realistic clouds and we also discuss the advantages and drawbacks of using a DNS approach as compared to an LES approach to study the subsiding shell.

Understanding how the droplet size distribution varies spatially and temporally in a cloud is a major challenge. The DSD is the defining characteristic of a cloud, determining how the cloud interacts with electromagnetic radiation, how fast precipitation will form, and so forth (Shaw 2003). In our simulation, all droplets have been initialized uniformly with a single radius between 10 and 20 μm. The droplet number concentration in our case varies between approximately 40 and 320 droplets per cubic centimeter. A concentration of 40 droplets per cubic centimeter can, for example, be found in clean marine clouds, whereas 320 droplets per cubic centimeter can, for example, be found in continental clouds. Although in our study different droplet sizes are considered, more realistic (i.e., polydisperse) droplet distributions would increase the applicability of this study.

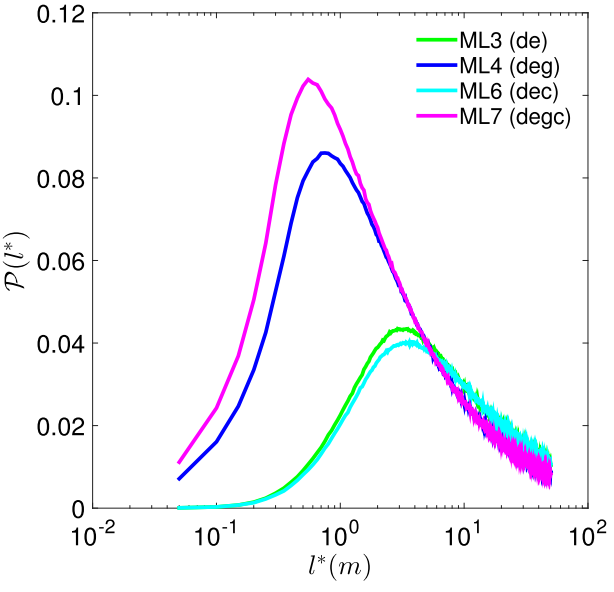

FIG. 6. Transition length scales at $t = 11$ s for simulations ML3–ML7.

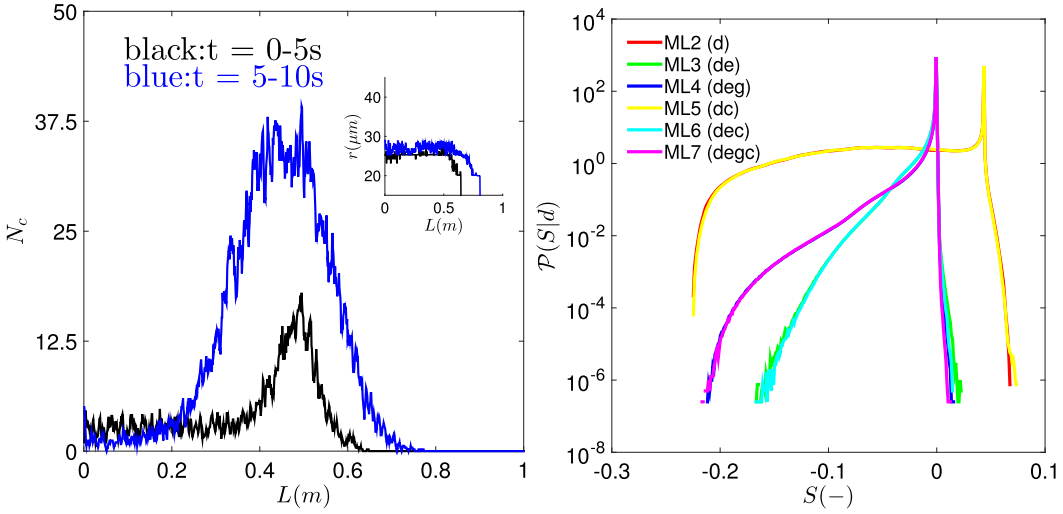

FIG. 7. (left) Number of collisions in simulation ML7 across the mixing layer accumulated for different time spans. The inset shows the maximum droplet radius. (right) Evolution of the collision kernel for simulations ML2–ML7.

Because the turbulence is heterogeneous, we must account for possible turbophoresis. Turbophoresis (Caporaloni et al. 1975) is the tendency for droplets to migrate in the direction of decreasing turbulence level. At the boundary of the computational domain, the wall-normal velocity and fluctuations are zero, reducing the local level of turbulence. Therefore droplets tend to cluster at the boundary of the domain in the cloud side of the simulation, which increases their local concentration and potentially increases the number of collisions. In the buoyancy profiles in Fig. 9 a wiggle is observed near the computational boundary inside the cloud, which is an effect of turbophoresis. During the first part of the simulations, the dissipation rate and turbulent intensity are low inside the cloud and most of the collisions occur at the cloud–environment interface; see Fig. 7 (left). In simulation ML7 no additional collisions are detected at the boundary of the computation domain resulting from turbophoresis. Additionally, coalesced droplets evaporate (see Fig. 5), which indicates that they reside near the cloud–environment interface. The effect of numerically induced turbophoresis is therefore considered to be very small in this study.

Our results show that gravity influences the behavior of droplets at the edge of a cloud. In our simulations, the environment is at rest with no turbulence present and droplets can fall freely. The dissipation rate is therefore zero in the environment, while in realistic clouds it is not. Recent measurements (Katzwinkel et al. 2014) show that in the environment, the dissipation rate is significantly lower than inside the cloud—from one to two orders of magnitude. The fluid Froude number in the environment (assuming $\langle\epsilon\rangle \approx 10^{-4}$) is on the order of 10^{-3}. According to Fouxon et al. (2014, manuscript submitted to *Phys. Rev. Lett.*,), when $\mathrm{Fr} \ll 1$ gravity dominates at an arbitrary Stokes number and the droplet velocity equals the droplet terminal velocity. We therefore believe that a nonturbulent environment does not qualitatively change our results.

The collision efficiency has not been taken into account. Including the collision efficiency reduces the chance of a successful collision (and coalescence). For our initial DSD of 20 μm, a collision efficiency of approximately 3.4% is found by Pinsky et al. (2001) for droplets of equal sizes. Smaller droplet sizes generally correspond to a lower collision efficiency. By taking into account the collision efficiency, a broadening of the DSD toward larger sizes would still occur, but at a much slower pace. The first droplets reaching a radius of 25 μm in simulation ML7 would not be within a few seconds but within approximately a minute. Hydrodynamic effects therefore alter the relative roles of the two competing effects of evaporation and coalescence at the cloud–environment interface, favoring evaporation as compared to present study. Nevertheless, helicopterborne measurements by Siebert et al. (2006) (Fig. 4) show an increase in large droplets near the edges of cumulus cloud with weak updrafts.

The size of the DNS domain is too small and the mixing layer simulated represents only an idealized small part of the cloud edge. Multiscale effects such as hypothesized by Shaw (2000), Lanotte et al. (2009), and Korolev et al. (2013) cannot be captured and the number of droplets is too low to allow ''lucky'' droplets (Kostinski and Shaw 2005). Also, no temperature lapse rate or pressure dependence on height has been taken

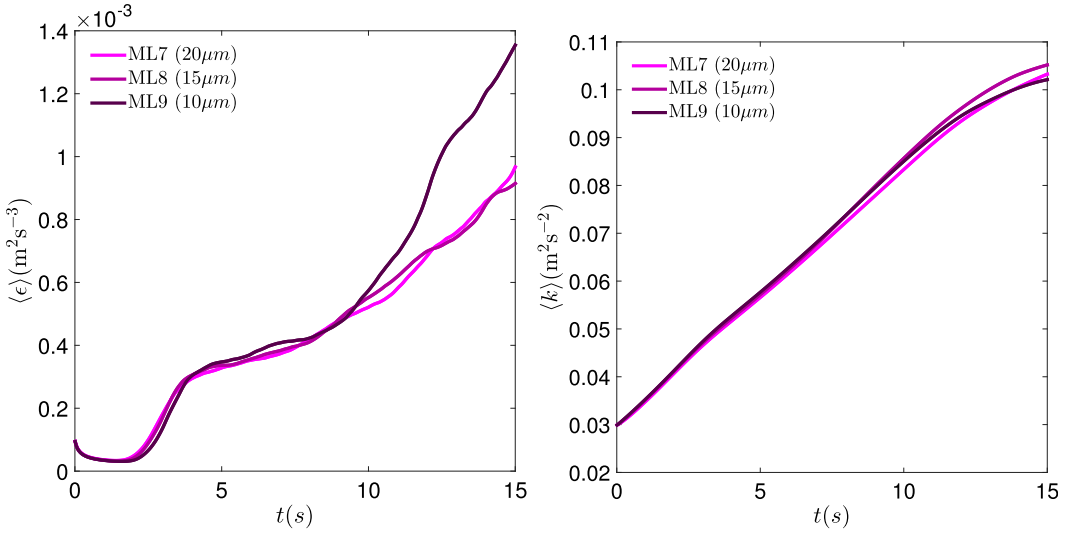

FIG. 8. Evolution of (left) the mean dissipation rate and (right) the mean turbulent kinetic energy during simulations ML7–ML9.

into account in the simulations. Some of these limitations can be overcome by using an LES model as has been previously done by Heus and Jonker (2008) and Jonker et al. (2008) [see Heus et al. (2010) for the numerical details of the Dutch Atmospheric LES]. While an LES model can capture the dynamics of an entire cloud, the model relies on its subgrid model to represent turbulent motion and transport that takes place at a scale smaller than the grid scale [25 m in the case of Heus and Jonker (2008) and Jonker et al. (2008)]. Droplets are represented by a two-moment bulk microphysics scheme (Seifert and Beheng 2001) and only information on the mean droplet radius is available, which provides limited information on the droplet growth at the edge of a cloud. A spectral bin model for cloud microphysics provides a more accurate description of the microphysical processes and could provide more insight in the evolution of the droplet size distribution, but it comes at a substantial computational cost of an additional scalar equation for every droplet size class considered [see review article of Khain et al. (2015) on bin microphysics versus bulk parameterization]. The study of Seifert et al. (2010) is an example of an LES simulation with a spectral bin model including a turbulent collision kernel (Ayala et al. 2008). A different approach for representing droplet microphysics in an LES is the Lagrangian cloud model (LCM), which is based on the concept of superdroplets, each representing a large number of real droplets of the same size (e.g., Riechelmann et al. 2012; Arabas and Shima 2013; Lee et al. 2014). Both a bin microphysics approach and an LCM can provide valuable information on the droplet size distribution but lack the accuracy to represent the turbulence and droplet dynamics down to the smallest scales. Choosing between DNS and LES to study the subsiding shell is therefore a trade-off between a very accurate, but idealized representation of a small part of the cloud shell versus a more realistic cloud simulation, but sacrificing small-scale microphysics and turbulent mixing. The approaches therefore complement each other.

6. Conclusions

In this paper we have investigated the droplet dynamics in a mixing layer using direct numerical simulation combined with a Lagrangian particle tracking algorithm as a paradigm for the lateral cloud–environment interface. Half of the computational domain represents the cloud and is initialized to be slightly warmer and moister than the environment with a representative number of 20-μm droplets. We have investigated the role of evaporation, gravity, coalescence, and the initial droplet size distribution on the intensity of the mixing layer and the evolution of the droplet size distribution.

Through a positive feedback loop, mixing of the droplets with environmental air induces evaporative cooling of the droplets, which results in a very characteristic subsiding shell (Heus and Jonker 2008; Jonker et al. 2008; Heus et al. 2009; Wang and Geerts 2010; Abma et al. 2013; Katzwinkel et al. 2014). As a consequence, stronger horizontal velocity gradients are found, which induces more mixing and evaporative cooling. A broadening of the droplet size distribution has been observed as a result of evaporation and coalescence, which increases the collision kernel.

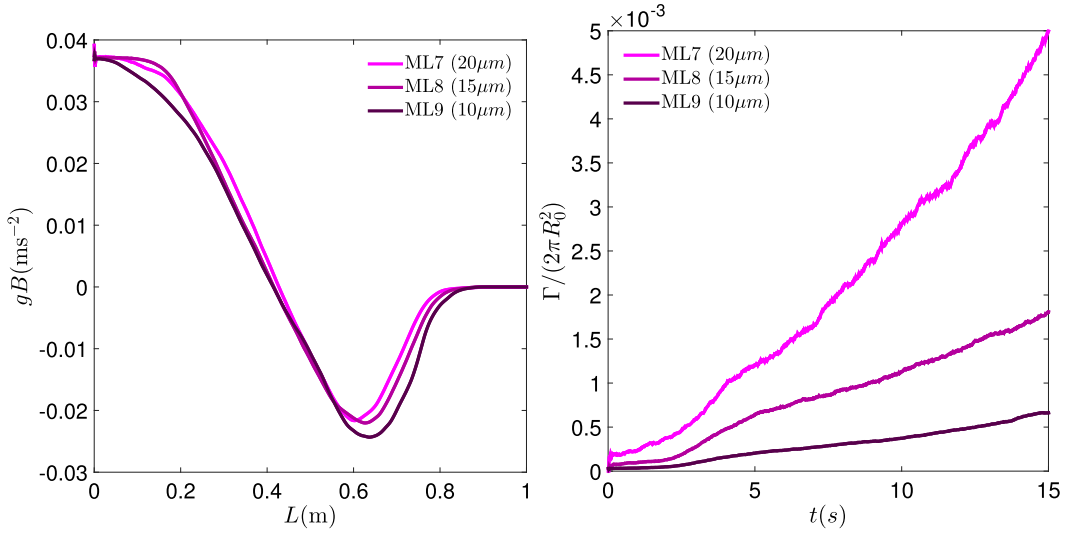

FIG. 9. (left) Average buoyancy profile across the mixing layer at $t = 11$ s for simulations ML7–ML9. (right) Evolution of the mean collision kernel normalized by the collisional cross section $2\pi R_0^2$, where R_0 is the initial droplet size.

Gravity acting on the droplets allows droplets in cloudy filaments detrained from the cloud to sediment and remain longer in the unsaturated environment. While this effect of gravity did not have a significant impact in our case on the mean evolution of the mixing layer, it does contribute to the broadening of the droplet size distribution and thereby significantly increases the collision rate. Although more collisions occur at the interface, this does not imply that the maximum droplet radius is larger at that location during the simulation.

By investigating the effect of the initial droplet size distribution on the evolution and the intensity of the mixing layer, we have found that for a constant amount of liquid water in the simulation a competition exists between evaporative cooling and dissipation of turbulent kinetic energy. Although more but smaller droplets result in more evaporative cooling, more droplets also increase small-scale fluctuations and thereby increase the dissipation rate. For the smallest droplets considered with a radius of 10 μm, we found that, although a more pronounced buoyancy dip was present, the increase in dissipation rate actually led to a decrease in the turbulent intensity of the mixing layer.

Care has to be taken when applying these results to realistic clouds. Not only is the size of the computational

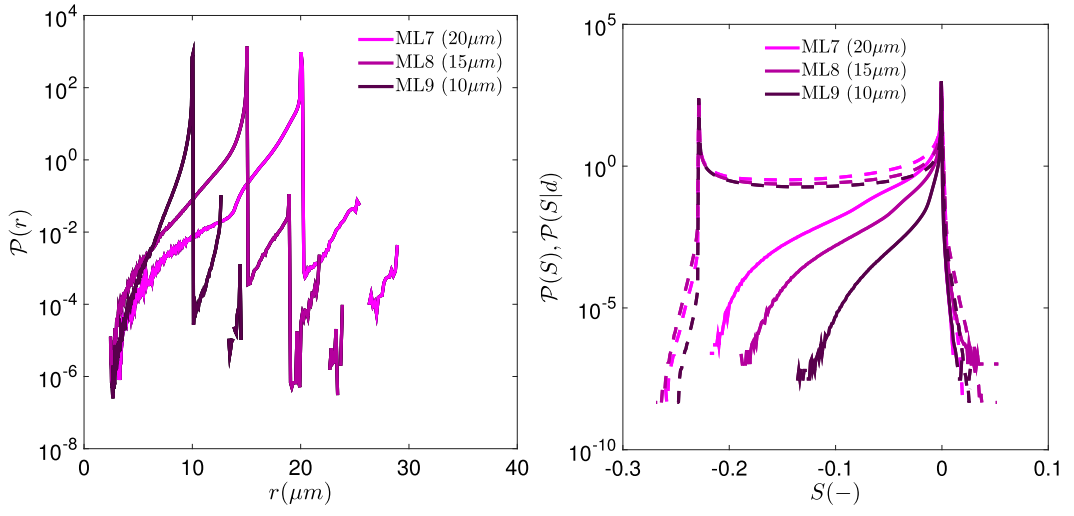

FIG. 10. (left) DSD of simulations ML7–ML9 after $t = 11$ s. (right) PDF of the supersaturation (dashed) and the PDF of the supersaturation conditionally sampled on the droplets locations (solid) at $t = 11$ s for simulations ML7–ML9.

domain much smaller than the size of a real cloud, but, by not taking into account the collision efficiency, the broadening of the droplet size distribution is substantially overestimated.

Acknowledgments. This work is part of the research program of the Foundation for Fundamental Research on Matter (FOM), which is part of the Netherlands Organisation for Scientific Research (NWO). This work was carried out on the Dutch national e-infrastructure with the support of the SURF Foundation.

REFERENCES

Abma, D., T. Heus, and J. P. Mellado, 2013: Direct numerical simulation of evaporative cooling at the lateral boundary of shallow cumulus clouds. *J. Atmos. Sci.*, **70**, 2088–2102, doi:10.1175/JAS-D-12-0230.1.

Alduchov, O. A., and R. E. Eskridge, 1996: Improved Magnus form approximation of saturation vapor pressure. *J. Appl. Meteor.*, **35**, 601–609, doi:10.1175/1520-0450(1996)035<0601:IMFAOS>2.0.CO;2.

Allen, P., and D. J. Tildesley, 1987: *Computer Simulation of Liquids*. Clarendon Press, 408 pp.

Andrejczuk, M., W. W. Grabowski, S. P. Malinowski, and P. K. Smolarkiewicz, 2004: Numerical simulation of cloud–clear air interfacial mixing. *J. Atmos. Sci.*, **61**, 1726–1739, doi:10.1175/1520-0469(2004)061<1726:NSOCAI>2.0.CO;2.

——, ——, ——, and ——, 2006: Numerical simulation of cloud–clear air interfacial mixing: Effects on cloud microphysics. *J. Atmos. Sci.*, **63**, 3204–3225, doi:10.1175/JAS3813.1.

——, ——, ——, and ——, 2009: Numerical simulation of cloud–clear air interfacial mixing: Homogeneous versus inhomogeneous mixing. *J. Atmos. Sci.*, **66**, 2493–2500, doi:10.1175/2009JAS2956.1.

Arabas, S., and S.-i. Shima, 2013: Large-eddy simulations of trade wind cumuli using particle-based microphysics with Monte Carlo coalescence. *J. Atmos. Sci.*, **70**, 2768–2777, doi:10.1175/JAS-D-12-0295.1.

Ashgriz, N., and J. Y. Poo, 1990: Coalescence and separation in binary collisions of liquid drops. *J. Fluid Mech.*, **221**, 183–204, doi:10.1017/S0022112090003536.

Ayala, O., B. Rosa, and L. P. Wang, 2008: Effects of turbulence on the geometric collision rate of sedimenting droplets. Part 2. Theory and parameterization. *New J. Phys.*, **10**, 075016, doi:10.1088/1367-2630/10/7/075016.

Babkovskaia, N., M. Boy, S. Smolander, S. Romakkaniemi, U. Rannik, and M. Kulmala, 2015: A study of aerosol activation at the cloud edge with high resolution numerical simulations. *Atmos. Res.*, **153**, 49–58, doi:10.1016/j.atmosres.2014.07.017.

Caporaloni, M., F. Tampieri, F. Trombetti, and O. Vittori, 1975: Transfer of particles in nonisotropic air turbulence. *J. Atmos. Sci.*, **32**, 565–568, doi:10.1175/1520-0469(1975)032<0565:TOPINA>2.0.CO;2.

Chen, M., K. Kontomaris, and J. B. McLaughlin, 1999: Direct numerical simulation of droplet collisions in a turbulent channel flow. Part I: Collision algorithm. *Int. J. Multiphase Flow*, **24**, 1079–1103, doi:10.1016/S0301-9322(98)00007-X.

Deardorff, J. W., 1980: Cloud top entrainment instability. *J. Atmos. Sci.*, **37**, 131–147, doi:10.1175/1520-0469(1980)037<0131:CTEI>2.0.CO;2.

Devenish, B. J., and Coauthors, 2012: Droplet growth in warm turbulent clouds. *Quart. J. Roy. Meteor. Soc.*, **138**, 1401–1429, doi:10.1002/qj.1897.

Falkovich, G., and A. Pumir, 2007: Sling effect in collisions of water droplets in turbulent clouds. *J. Atmos. Sci.*, **64**, 4497–4505, doi:10.1175/2007JAS2371.1.

——, A. Fouxon, and M. G. Stepanov, 2002: Acceleration of rain initiation by cloud turbulence. *Nature*, **419**, 151–154, doi:10.1038/nature00983.

Gatignol, R., 1983: The Faxén formulas for a rigid particle in an unsteady non-uniform Stokes-flow. *J. Mec. Theor. Appl.*, **2**, 143–160.

Grabowski, W. W., 1989: Numerical experiments on the dynamics of the cloud–environment interface: Small cumulus in a shear-free environment. *J. Atmos. Sci.*, **46**, 3513–3541, doi:10.1175/1520-0469(1989)046<3513:NEOTDO>2.0.CO;2.

——, and L.-P. Wang, 2013: Growth of cloud droplets in a turbulent environment. *Annu. Rev. Fluid Mech.*, **45**, 293–324, doi:10.1146/annurev-fluid-011212-140750.

——, M. Andrejczuk, and L. P. Wang, 2011: Droplet growth in a bin warm-rain scheme with Twomey CCN activation. *Atmos. Res.*, **99**, 290–301, doi:10.1016/j.atmosres.2010.10.020.

Hall, W. D., 1980: A detailed microphysical model within a two-dimensional dynamic framework: Model description and preliminary results. *J. Atmos. Sci.*, **37**, 2486–2507, doi:10.1175/1520-0469(1980)037<2486:ADMMWA>2.0.CO;2.

Heus, T., and H. J. J. Jonker, 2008: Subsiding shells around shallow cumulus clouds. *J. Atmos. Sci.*, **65**, 1003–1018, doi:10.1175/2007JAS2322.1.

——, C. F. J. Pols, H. J. J. Jonker, H. E. den Akker, and D. H. Lenschow, 2009: Observational validation of the compensating mass flux through the shell around cumulus clouds. *Quart. J. Roy. Meteor. Soc.*, **135**, 101–112, doi:10.1002/qj.358.

——, and Coauthors, 2010: Formulation of the Dutch Atmospheric Large-Eddy Simulation (DALES) and overview of its applications. *Geosci. Model Dev.*, **3**, 415–444, doi:10.5194/gmd-3-415-2010.

Jonas, P. R., 1996: Turbulence and cloud microphysics. *Atmos. Res.*, **40**, 283–306, doi:10.1016/0169-8095(95)00035-6.

Jones, W. P., S. Lyra, and A. J. Marquis, 2010: Large eddy simulation of a droplet laden turbulent mixing layer. *Int. J. Heat Fluid Flow*, **31**, 93–100, doi:10.1016/j.ijheatfluidflow.2009.10.001.

Jonker, H. J. J., T. Heus, and P. P. Sullivan, 2008: A refined view of vertical mass transport by cumulus convection. *Geophys. Res. Lett.*, **35**, L07810, doi:10.1029/2007GL032606.

——, M. van Reeuwijk, P. P. Sullivan, and E. G. Patton, 2013: On the scaling of shear-driven entrainment: A DNS study. *J. Fluid Mech.*, **732**, 150–165, doi:10.1017/jfm.2013.394.

Katzwinkel, J., H. Siebert, T. Heus, and R. a. Shaw, 2014: Measurements of turbulent mixing and subsiding shells in trade wind cumuli. *J. Atmos. Sci.*, **71**, 2810–2822, doi:10.1175/JAS-D-13-0222.1.

Khain, A., M. Pinsky, T. Elperin, N. Kleeorin, I. Rogachevskii, and A. Kostinski, 2007: Critical comments to results of investigations of drop collisions in turbulent clouds. *Atmos. Res.*, **86**, 1–20, doi:10.1016/j.atmosres.2007.05.003.

——, and Coauthors, 2015: Representation of microphysical processes in cloud-resolving models: Spectral (bin) microphysics versus bulk parameterization. *Rev. Geophys.*, **53**, 247–322, doi:10.1002/2014RG000468.

Korczyk, P., S. P. Malinowski, and T. A. Kowalewski, 2006: Mixing of cloud and clear air in centimeter scales observed in laboratory

by means of Particle Image Velocimetry. *Atmos. Res.*, **82**, 173–182, doi:10.1016/j.atmosres.2005.09.009.

Korolev, A., M. Pinsky, and A. Khain, 2013: A new mechanism of droplet size distribution broadening during diffusional growth. *J. Atmos. Sci.*, **70**, 2051–2071, doi:10.1175/JAS-D-12-0182.1.

Kostinski, A. B., and R. A. Shaw, 2005: Fluctuations and luck in droplet growth by coalescence. *Bull. Amer. Meteor. Soc.*, **86**, 235–244, doi:10.1175/BAMS-86-2-235.

Kumar, B., J. Schumacher, and R. A. Shaw, 2013: Cloud microphysical effects of turbulent mixing and entrainment. *Theor. Comput. Fluid Dyn.*, **27**, 361–376, doi:10.1007/s00162-012-0272-z.

——, ——, and ——, 2014: Lagrangian mixing dynamics at the cloudy–clear air interface. *J. Atmos. Sci.*, **71**, 2564–2580, doi:10.1175/JAS-D-13-0294.1.

Lanotte, A. S., A. Seminara, and F. Toschi, 2009: Cloud droplet growth by condensation in homogeneous isotropic turbulence. *J. Atmos. Sci.*, **66**, 1685–1697, doi:10.1175/2008JAS2864.1.

Lasher-Trapp, S. G., W. A. Cooper, and A. M. Blyth, 2005: Broadening of droplet size distributions from entrainment and mixing in a cumulus cloud. *Quart. J. Roy. Meteor. Soc.*, **131**, 195–220, doi:10.1256/qj.03.199.

Lee, J., Y. Noh, S. Raasch, T. Riechelmann, and L.-P. Wang, 2014: Investigation of droplet dynamics in a convective cloud using a Lagrangian cloud model. *Meteor. Atmos. Phys.*, **124**, 1–21, doi:10.1007/s00703-014-0311-y.

Lehmann, K., H. Siebert, and R. A. Shaw, 2009: Homogeneous and inhomogeneous mixing in cumulus clouds: Dependence on local turbulence structure. *J. Atmos. Sci.*, **66**, 3641–3659, doi:10.1175/2009JAS3012.1.

Maxey, M. R., and J. J. Riley, 1983: Equation of motion for a small rigid sphere in a nonuniform flow. *Phys. Fluids*, **26**, 883–889, doi:10.1063/1.864230.

Mellado, J. P., 2010: The evaporatively driven cloud-top mixing layer. *J. Fluid Mech.*, **660**, 5–36, doi:10.1017/S0022112010002831.

——, B. Stevens, H. Schmidt, and N. Peters, 2009: Buoyancy reversal in cloud-top mixing layers. *Quart. J. Roy. Meteor. Soc.*, **135**, 963–978, doi:10.1002/qj.417.

Perrin, V. E., and H. J. J. Jonker, 2014: Preferred location of droplet collisions in turbulent flows. *Phys. Rev.*, **89E**, 33005, doi:10.1103/PhysRevE.89.033005.

Pinsky, M. B., and A. P. Khain, 2002: Effects of in-cloud nucleation and turbulence on droplet spectrum formation in cumulus clouds. *Quart. J. Roy. Meteor. Soc.*, **128**, 501–533, doi:10.1256/003590002321042072.

——, ——, and M. Shapiro, 1999: Collisions of small drops in a turbulent flow. Part I: Collision efficiency. Problem formulation and preliminary results. *J. Atmos. Sci.*, **56**, 2585–2600, doi:10.1175/1520-0469(1999)056<2585:COSDIA>2.0.CO;2.

——, ——, and ——, 2001: Collision efficiency of drops in a wide range of Reynolds numbers: Effects of pressure on spectrum evolution. *J. Atmos. Sci.*, **58**, 742–764, doi:10.1175/1520-0469(2001)058<0742:CEODIA>2.0.CO;2.

——, I. P. Mazin, A. Korolev, and A. Khain, 2013: Supersaturation and diffusional droplet growth in liquid clouds. *J. Atmos. Sci.*, **70**, 2778–2793, doi:10.1175/JAS-D-12-077.1.

Pruppacher, H. R., and J. D. Klett, 1978: *Microphysics of Clouds and Precipitation*. Springer, 714 pp.

Qian, J., and C. K. Law, 1997: Regimes of coalescence and separation in droplet collision. *J. Fluid Mech.*, **331**, 59–80, doi:10.1017/S0022112096003722.

Riechelmann, T., Y. Noh, and S. Raasch, 2012: A new method for large-eddy simulations of clouds with Lagrangian droplets including the effects of turbulent collision. *New J. Phys.*, **14**, 065008, doi:10.1088/1367-2630/14/6/065008.

Sedunov, Y. S., and P. Greenberg, 1974: *Physics of Drop Formation in the Atmosphere*. Wiley, 234 pp.

Seifert, A., and K. D. Beheng, 2001: A double-moment parameterization for simulating autoconversion, accretion and self-collection. *Atmos. Res.*, **59–60**, 265–281, doi:10.1016/S0169-8095(01)00126-0.

——, L. Nuijens, and B. Stevens, 2010: Turbulence effects on warm-rain autoconversion in precipitating shallow convection. *Quart. J. Roy. Meteor. Soc.*, **136**, 1753–1762, doi:10.1002/qj.684.

Shaw, R. A., 2000: Supersaturation intermittency in turbulent clouds. *J. Atmos. Sci.*, **57**, 3452–3456, doi:10.1175/1520-0469(2000)057<3452:SIITC>2.0.CO;2.

——, 2003: Particle-turbulence interaction in atmospheric clouds. *Annu. Rev. Fluid Mech.*, **35**, 183–227, doi:10.1146/annurev.fluid.35.101101.161125.

Siebert, H., K. Lehmann, M. Wendisch, H. Franke, R. Maser, D. Schell, E. Wei Saw, and R. A. Shaw, 2006: Probing finescale dynamics and microphysics of clouds with helicopter-borne measurements. *Bull. Amer. Meteor. Soc.*, **87**, 1727–1738, doi:10.1175/BAMS-87-12-1727.

Tölle, M. H., and S. K. Krueger, 2014: Effects of entrainment and mixing on droplet size distributions in warm cumulus clouds. *J. Adv. Model. Earth Syst.*, **6**, 281–299, doi:10.1002/2012MS000209.

Vaillancourt, P. A., M. K. Yau, and W. W. Grabowski, 2001: Microscopic approach to cloud droplet growth by condensation. Part I: Model description and results without turbulence. *J. Atmos. Sci.*, **58**, 1945–1964, doi:10.1175/1520-0469(2001)058<1945:MATCDG>2.0.CO;2.

——, ——, P. Bartello, and W. W. Grabowski, 2002: Microscopic approach to cloud droplet growth by condensation. Part II: Turbulence, clustering, and condensational growth. *J. Atmos. Sci.*, **59**, 3421–3435, doi:10.1175/1520-0469(2002)059<3421:MATCDG>2.0.CO;2.

Wallace, J. M., and P. V. Hobbs, 2006: *Atmospheric Science: An Introductory Survey*. 2nd ed. Elsevier, 504 pp.

Wang, Y., and B. Geerts, 2010: Humidity variations across the edge of trade wind cumuli: Observations and dynamical implications. *Atmos. Res.*, **97**, 144–156, doi:10.1016/j.atmosres.2010.03.017.

Wilkinson, M., and B. Mehlig, 2005: Caustics in turbulent aerosols. *Europhys. Lett.*, **71**, 186, doi:10.1209/epl/i2004-10532-7.

——, ——, and V. Bezuglyy, 2006: Caustic activation of rain showers. *Phys. Rev. Lett.*, **97**, 048501, doi:10.1103/PhysRevLett.97.048501.

Woittiez, E. J. P., H. J. J. Jonker, and L. M. Portela, 2009: On the combined effects of turbulence and gravity on droplet collisions in clouds: A numerical study. *J. Atmos. Sci.*, **66**, 1926–1943, doi:10.1175/2005JAS2669.1.